RESEARCH ARTICLE

Multistep Crystallization Pathways in the Ambient-Temperature Synthesis of a New Alkali-Activated Binder

Marcel Maslyk, Tobias Gäb, Galina Matveeva, Phil Opitz, Mihail Mondeshki, Yasar Krysiak, Ute Kolb, and Wolfgang Tremel*

Concrete is the most prevalent manufactured material that has shaped the built environment, but the high-temperature production of cement, the main component of concrete, has a massive carbon footprint. It is shown that CO_2 emissions during clinker production of cement can be circumvented by a metathesis reaction at room temperature in ball-mills, where the cement clinker is replaced by non-calcined limestone and alkali-activated binders/geopolymers. An amorphous intermediate (aNaSiCC) containing a random mixture of the ionic constituents in "molecular" dispersion is formed by mechanochemical activation of $CaCO_3$ and Na_2SiO_3. This allows molecular transport during crystallization and low activated reactions, as precipitation of solids from liquids (nucleation limited and kinetically controlled) and solid-state transformations (diffusion-limited and thermodynamically controlled) have equal weight. Several steps of the hydration reaction could be resolved. Activating the amorphous aNaSiCC precursor with NaOH leads to a C—S—H-like phase with a C/S ratio of ≈1 containing some sodium. The carbonate components pass through a multistep crystallization from aNaSiCC via pirssonite and gaylussite to monohydrocalcite. The findings help unravel the interplay between thermodynamics and kinetics in complex reactions of alkali-activated binders and for $CaCO_3$ crystallization in industrial and geochemical settings, where dissolved silicate is always involved.

M. Maslyk, T. Gäb, G. Matveeva, P. Opitz, M. Mondeshki, U. Kolb, W. Tremel
Department Chemie
Johannes Gutenberg-Universität
Duesbergweg 10–14, D-55099 Mainz, Germany
E-mail: tremel@uni-mainz.de
Y. Krysiak
Institut für Anorganische Chemie
Gottfried Wilhelm Leibniz Universität
Callinstraße 3–9, D-30167 Hannover, Germany
U. Kolb
Institut für Angewandte Geowissenschaften
Technische Universität Darmstadt
Schnittspahnstraße 9, 64287 Darmstadt, Germany

1. Introduction

Mitigating the environmental consequences of anthropogenic CO_2 emissions is one of the major challenges of this century. For every ton of cement that is produced, one ton of greenhouse gases is released into the atmosphere, and the production of Portland cement accounts for ≈8% of anthropogenic CO_2 release.[1] Portland cements contain ground cement clinker, basically calcium silicates and aluminates, produced from limestone and other components in a high-temperature process with the release of CO_2, and then mixed with a sulfate carrier that serves to control solidification. Promising approaches to offset some of the massive carbon dioxide emissions from cement in clinker production include replacing Portland clinker with non-calcined limestone ($CaCO_3$), a readily available Ca source, or using alkali-activated binders/geopolymers as Si source for cement.[2,3] Alkali-activated binders and geopolymers can be distinguished according to the calcium content in the precursor and the phases of the resulting binder. Low-calcium systems tend to produce binders such as geopolymers, which may contain sodium aluminosilicate hydrate (N—A—S—H) gels, while high-calcium systems form alkali-activated binders containing phases like calcium silicate hydrate (C—S—H) or calcium aluminosilicate hydrate (C—A—S—H) gels.[4,5] Still, the reaction of calcium carbonate in alkali-activated/geopolymer systems,[6] in particular the reaction mechanisms, have rarely been studied. Firdous et al.[7] showed that calcium carbonate reacts partially with sodium silicate solutions by forming a C—S—H phase, which is likely to contain some sodium.

Mineral additions in cements as supplementary cementitious materials are known to have accelerating effects on cement hydration.[8,9] This is due, among others, to the distribution of the nucleation sites.[10] The use of up to 5%wt limestone in Portland cement as reactive filler material leads to the question of whether amorphous calcium carbonate could be used as an alternative activated precursor as it alters the dissolution and precipitation reactions and thus reduces CO_2 emissions.[11] Pure calcium carbonate is the textbook model system to study crystallization from solution at a molecular level. In ambient

**ADVANCED
SCIENCE NEWS**

www.advancedsciencenews.com

**ADVANCED
FUNCTIONAL
MATERIALS**

www.afm-journal.de

conditions, calcium carbonate exists in three anhydrous (calcite, aragonite, and vaterite)[12,13] and three hydrous (ikaite, monohydrocalcite, hemicarbonate) polymorphs[14–16] and in amorphous forms (ACC).[17] Studies on calcium carbonate, in particular ACC, have witnessed major advances in our comprehension of the early stages of crystallization.[18–21] Liquid-like precursors to ACC and so-called prenucleation species have been reported depending on the crystallization conditions.[22–25] Much of our current understanding of ACC comes from biomineral studies. Biogenic ACC has been classified as stable and hydrated (with an approximate composition $CaCO_3$ x H_2O) or transient and anhydrous.[17] A stepwise transformation of ACC to $CaCO_3$ is assumed although the exact mechanistic pathways remain unclear considering diffusion coefficients, mobility, and hydration energy of the divalent ions.[26–28] While anhydrous ACC is stable in the presence of water,[24] hydrated ACC crystallizes rapidly, which makes the process difficult to monitor.[29–32]

The crystallization of hydrated ACC may be slowed down by i) reducing the water concentration or ii) with matrix materials. Silica as "inert" matrix prevents ACC crystallization. Silica coatings prepared by mixing $CaCl_2$ with Na_2CO_3/Na_2SiO_3 stabilize $CaCO_3$ prenucleation clusters[33] or retard ACC nucleation by setting a barrier to water diffusion.[34,35] This allowed monitoring the polymorphic transformations of ACC. Crystallization experiments conducted in the absence of silica showed a conversion to calcite via vaterite and aragonite, while encapsulation in a silica matrix[36] containing a mixture of different silicate species due to its preparation in diluted "water glass", induced marked changes in the temporal evolution of the polymorphic fractions.[37]

This work investigates the formal metathesis reaction of solid calcium carbonate with solid sodium metasilicate at room temperature and its significance for geopolymer/alkali-activated binders. An amorphous solid solution of $CaCO_3$ and Na_2SiO_3 is used as "activated precursor". To this end, the reactants, $CaCO_3$ and Na_2SiO_3, were ball-milled into a reactive amorphous form in which the components of the desired product are mixed at the molecular level. This milling process allows an industrial scale implementation while potentially reducing undesired CO_2 emissions in combination with conventional production processes. Furthermore, we show that by deliberate retardation of the crystallization process, a stepwise transformation via metastable phases can be traced. Solid-state reactions are typically very slow and require long reactions times and high temperatures, because the transport lengths of the reacting species are in the order of micrometers, while the diffusion coefficients typically range from 10^{-12} to 10^{-16} cm^2 s^{-1}.[38] Diffusional control can be circumvented by reducing transport distances to molecular dimensions by dispersing the components at a molecular level or by increasing defect concentrations.[39–41] This "activated precursor" containing a statistically "frozen" mixture of educts was generated mechanochemically.[42]

Different from solid-state reactions, where diffusion is intrisically slow, and solution reactions, where diffusion is fast, water/acetonitrile mixtures were then used to retard the crystallization process while still allowing structural reorganization to occur.[43] Our approach experimentally mimics the "simulated annealing" concept, which has been employed for predicting inorganic solids and their crystal structures[44] and allows to explore the energy landscape of a reaction system by controlling

supersaturation via solvent concentration. This allows to follow the reaction pathway analytically and structurally through a number of intermediates in order to mechanistically understand the formation of alkali-activated binders.

X-ray powder diffraction (XRD) and total scattering, transmission electron microscopy (TEM) combined with automated diffraction tomography (ADT), Fourier transform infrared spectroscopy (FTIR), and multinuclear magic angle spinning (MAS) nuclear magnetic resonance (NMR) spectroscopy were used to elucidate the reaction kinetics, phase evolution and local structure at the primary stages of the reaction for crystalline and especially non-crystalline intermediates.

The sequence of events is outlined in **Figure 1**. In a first "activation" step, calcium carbonate and sodium metasilicate were ball-milled to a randomly "frozen" non-equilibrium intermediate, sodium-calcium carbonate/silicate (aNaSiCC). The corresponding reaction of calcium carbonate with Na_2CO_3 (the carbon analog of Na_2SiO_3) yielded amorphous sodium calcium carbonate (aNaCC). Reaction of aNaSiCC with water under controlled conditions initiates a cascade of reactions leading to monohydrocalcite ($CaCO_3$ × H_2O) via the metastable intermediates pirssonite ($Na_2Ca(CO_3)_2$ × $2H_2O$) and gaylussite ($Na_2Ca(CO_3)_2$ × $5H_2O$) in the Ca branch. The reaction starting from silicate-free aNaCC leads only to the formation of calcite without incorporation of water. The formation of pirssonite and gaylussite indicates a reorganization of the sodium and calcium cations, thus promoting the formation of a calcium silicate precursor in the Si branch, which likely contains some sodium and reacts to a C−S−H-type phase by activation with NaOH. Ca/Si (C/S) ratios between 0.67 and 1.5 are consistent with a defect tobermorite structure.[45] Our findings are a step forward in unraveling the reaction mechanisms involved in the preparation and formation of alkali-activated binders.
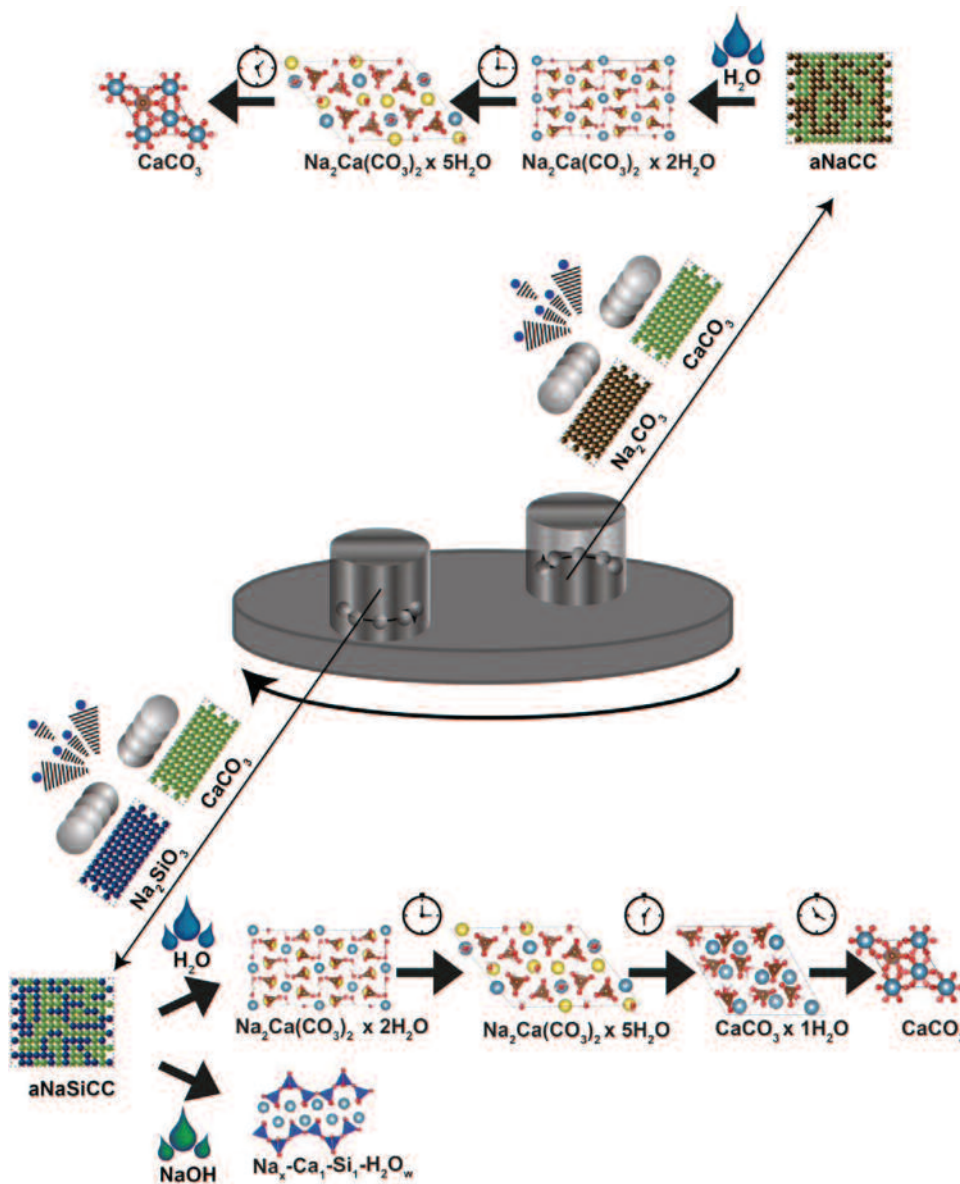
2. Results and Discussion

2.1. Synthesis

2.1.1. Mechanochemical Activation

We investigated the mechanochemical activation of calcite with sodium metasilicate (Na_2SiO_3) and sodium carbonate (Na_2CO_3) in a planetary ball mill. Recrystallization in water led to mixed sodium/calcium carbonate hydrates (vide infra). This indicates that a high sodium content in calcium carbonate plays a crucial role in recrystallization and hydration. Small amounts ($7.5\%_w$) of Na_2CO_3 have been shown to induce amorphization of calcite in mechanochemical reactions.[40]

As calcium silicate hydrate (C−S−H), the main constituent of hydrated cements, can contain a broad range of Ca/Si ratios[46] we reacted equimolar amounts of $CaCO_3$ with Na_2SiO_3 and its carbon analog Na_2CO_3 to compare the outcome of the mechanochemical reactions. The presence of only one $CaCO_3$/Na_2SiO_3 (aNaSiCC, Na_2SiO_3 substitution) or two $CaCO_3$/Na_2CO_3 (aNaCC, Na_2CO_3 substitution) modulations in the powder X-ray diffraction patterns of the amorphous products aNaSiCC and aNaCC (**Figure 2**A) and the absence of any electron diffraction (ED) spots in TEM (Figure 2B) are compatible

**ADVANCED
SCIENCE NEWS**

www.advancedsciencenews.com

**ADVANCED
FUNCTIONAL
MATERIALS**

www.afm-journal.de

Figure 1. Overview of the mechanochemical preparation of the amorphous intermediates of $CaCO_3$ and $NaCO_3$ (aNaCC) or $CaCO_3$ and $NaSiO_3$ (aNaSiCC) and the reaction paths of the setting reactions of aNaCC and aNaSiCC with water. The hydration reaction of aNaCC with H_2O leads to the crystallization of calcite (top). The reaction of aNaSiCC on the carbonate reaction branch leads to monohydrocalcite ($CaCO_3 \times H_2O$), on the silicate reaction branch after NaOH activation to the formation of C—S—H (bottom).

with a loss of long-range order on the micro- and nanoscale in both products.

FTIR spectroscopy is a useful tool to probe local environments.[47] FTIR spectra of aNaSiCC and aNaCC (Figure 2C) show four characteristic carbonate bands (symmetric stretch v_1 1070 cm^{-1}; out-of-plane deformation v_2, 865 cm^{-1}; asymmetric stretch v_3, 1377 cm^{-1}; in-plane-deformation v_4, 695 and 717 cm^{-1}). The (symmetry forbidden) v_1 mode, the splitting of the v_3 and v_4 modes and the distinct broadening of the vibration bands of the CO_3^{2-} anion are strong indicators for the evolution of the chemical environment due to amorphization.[48] The bands of aNaSiCC are shifted to higher wavenumbers compared to aNaCC. This is most pronounced for the v_3 mode

and in line with the bond energies for the CO_3^{2-} and SiO_3^{2-} anions. The incorporation of silicate in aNaSiCC is marked by a broadband in the range from 1100 to 900 cm^{-1} associated with the symmetric and asymmetric stretching modes of the Si—O—Si (1050 cm^{-1}) and Si—O$^-$ (950 cm^{-1}) units.[49,50]

Structural information about the short-range order in amorphous aNaSiCC was obtained by solid-state (ss) MAS-NMR.[51] A comparison of the ^{13}C NMR spectra of calcite ($\delta = 168.2$ ppm, full width at half maximum (FWHM) = 30 Hz), aNaCC ($\delta = 169.4$ ppm, FWHM = 340 Hz), and aNaSiCC ($\delta = 170.16$ ppm, FWHM = 334 Hz) (Figure 2D) shows a slight shift and distinct broadening of the CO_3^{2-} signals in aNaSiCC and aNaCC compared to calcite.
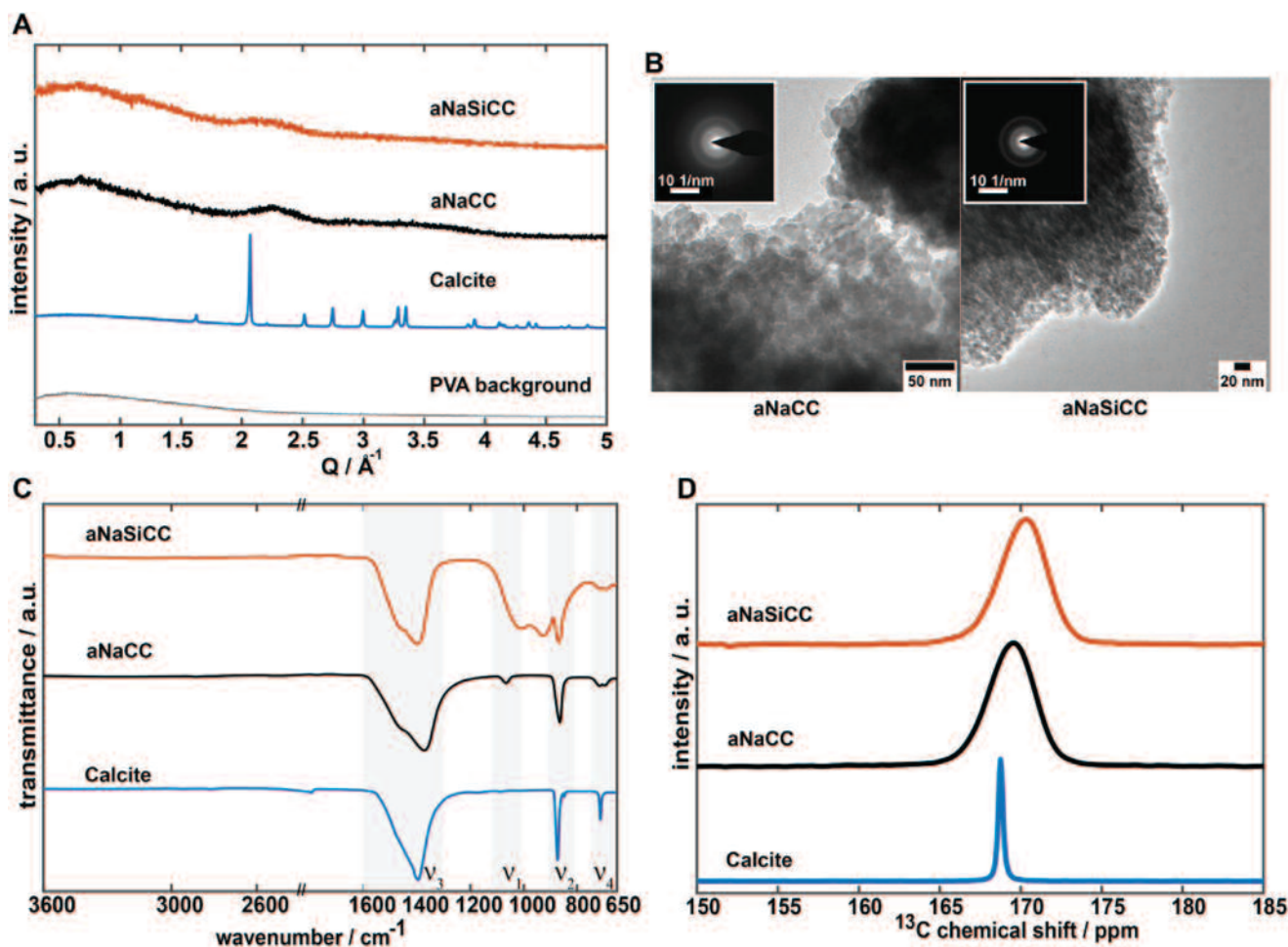
Figure 2. A) PXRD diffractograms after full amorphization (grey line: poly(vinyl alcohol) background; blue line: Calcite black line: aNaSiCC; red line: aNaCC). B) TEM images and SAED pattern of aNaSiCC and aNaCC after complete amorphization. Insets show the corresponding SAED patterns. C) IR spectra of calcite (blue line), aNaSiCC (red line), and aNaCC (black line). D) ^{13}C NMR spectra of calcite (blue line), aNaCC (black line), aNaSiCC (red line).

While the C−O length in calcite is 1.25 Å[52] shorter distances of 1.18 Å are observed in Na_2CO_3.[53] This leads to stronger deshielding and thus a slight downfield shift of 2.2 ppm compared to the ^{13}C NMR shifts of calcite (168.5 ppm) and sodium carbonate (170.7 ppm). A previous study found that the amorphization of calcite is complete with only 7% sodium carbonate.[40] It is accompanied by signal broadening without a change in the ^{13}C carbonate shift.

Higher amounts of Na_2CO_3 lead to a slight change of ≈1 ppm in the ^{13}C shift (signal at 169.5 ppm for aNaCC). This average ^{13}C shift (between the ^{13}C shifts of Na_2CO_3 and calcite) may be due to a statistical distribution of Na^+ and Ca^{2+} cations around the CO_3^{2-} counter ion, resulting in a decrease in the average C−O length, in agreement with the differences in experimental FTIR data (vide supra). Surprisingly, a comparable ^{13}C shift was found as in pure Na_2CO_3 (170.5 ppm), implying that the local electronic environment of the CO_3^{2-} carbon atom in aNaSiCC and crystalline Na_2CO_3 is virtually identical even in the disordered state. This indicates an association of Na^+ and CO_3^{2-} ions or the charge compensation of Ca^{2+} and SiO_3^{2-} ions, which will be addressed in more detail below.

2.1.2. Kinetics of Mechanochemical Activation Reaction

In addition to the structure of the amorphous intermediates aNaCC and aNaSiCC, the formation mechanism during the milling reaction is of special interest. Since diffraction methods cannot provide meaningful information for amorphous products, the vibrational signatures of the carbonate groups and their ^{13}C NMR resonance signals were used as local probes. Changes in the local environments during the amorphization of aNaSiCC and aNaCC were monitored by taking "snapshots" of the products, that is, interrupting the milling at specified time intervals and recording FTIR and ^{13}C-NMR spectra ex situ.

The evolution of the FTIR spectra was monitored semiquantitatively using Lambert–Beer's law $A = -\log_{10}(T)$.(**Figure 3**A) The broadening and the shift of the v_2 bands (inset Figure 3A) were used to follow the transition from calcite ($v_2 = 873$ cm^{-1}) to the amorphous phases ($v_2 = 861$ cm^{-1} for aNaSiCC; $v_2 = 858$ cm^{-1} for aNaCC) using a bimodal Pseudo–Voigt function. After 450 min of grinding, the samples were X-ray amorphous as no changes occurred in the FTIR spectra and the diffractograms were free of reflections. Thus, the crystallinity
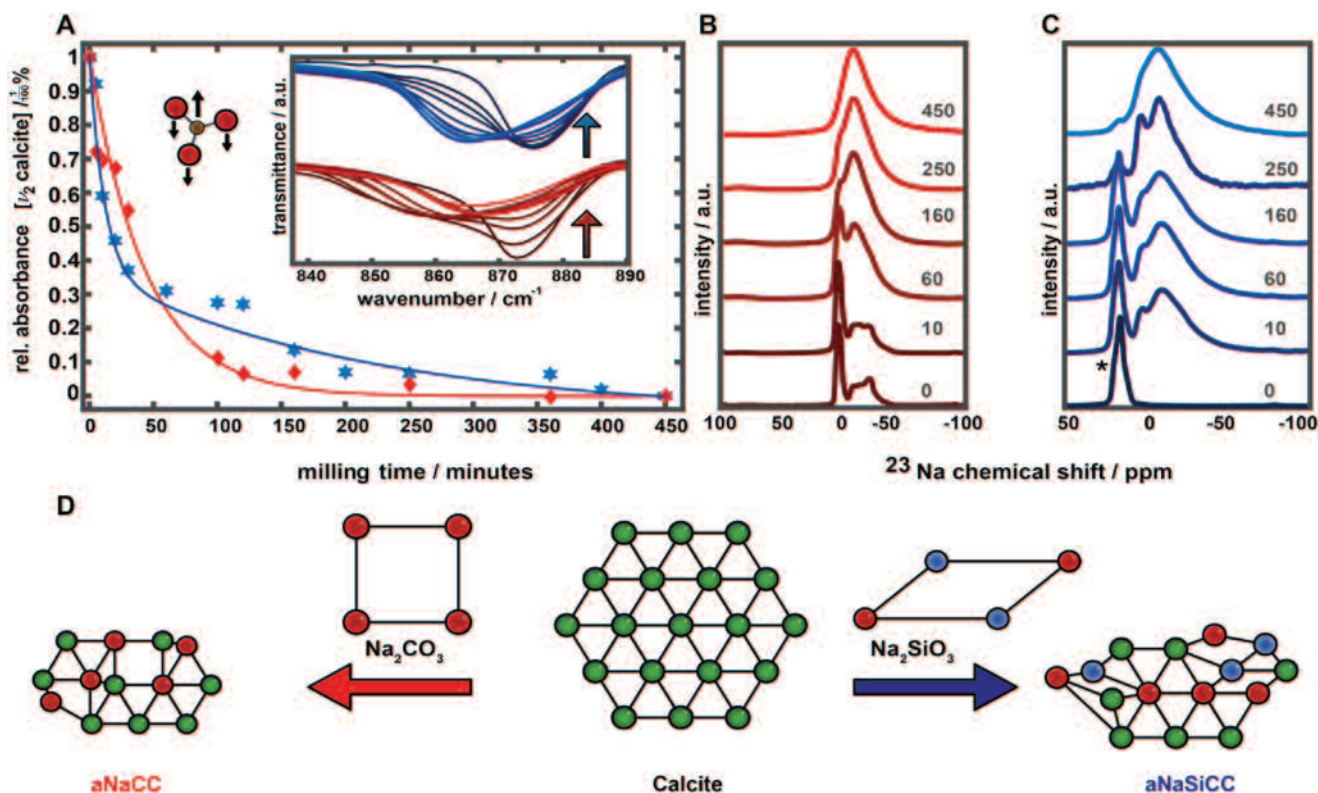
Figure 3. A) Exponential fits to the FTIR spectra for the amorphization of aNaCC (red line) and aNaSiCC (blue line) obtained by infrared spectroscopy. The inset shows the evolution of the v_2 band (narrow: dark blue /dark red, broad: light blue /light red). B,C) Time-dependent ^{23}Na MAS NMR signal after different milling times (red: aNaCC; blue: aNaSiCC). D) Scheme illustrating how the incorporation of sodium and silicate ions lead to disorder and eventually to a lack of long-range order.

at this time was set to "0%". By comparing the intensities from the respective fits with the v_2 mode of calcite (100% at t = 0) we observed an exponential loss of crystallinity (Figure 3A). The amorphization for aNaCC was faster than of NaSiCC. It was nearly complete after 300 min, whereas the amorphization for sodium silicate required a full run of 450 min. This could be monitored from the change in the Na environment during milling by ^{23}Na MAS NMR (Figure 3B). Its quadrupole moment (I = 3/2) makes ^{23}Na a suitable probe for changes in the local electronic environment. Still, the interpretation of the spectra is more complex due to the additional second-order quadrupole interactions.[54,55] NMR spectra of amorphous systems are characterized by broad resonances lacking the characteristic quadrupole pattern. The ^{23}Na spectrum of sodium metasilicate (Figure 3B, blue spectrum at t = 0) shows only one signal at 16.3 ppm with an FWHM of 600 Hz, which indicates a slightly distorted trigonal bypyramidal environment with an average Na−O distance of 2.37 Å.[56] Due to the high symmetry, the quadrupole coupling constant is relatively low leading to a sharp resonance. For Na_2CO_3 (Figure 3B, red spectrum at t = 0) one sharp signal at 3.8 ppm with an FWHM of 530 Hz and one broadened signal at −21.3 ppm with an FWHM of 2100 Hz appear because of the different sodium sites in Na_2CO_3.[57]

While the narrow line is associated with a highly symmetric octahedral coordination (CN 6), the broadened signal originates from a ninefold coordination of sodium (CN 9). A decrease in Na−O bond lengths is correlated with a high-field

shift occurring for mean distances of 2.35 Å in octahedral and 2.70 Å in ninefold coordination of sodium carbonate.[58] The amorphization of Na_2SiO_3 is a process associated with the generation of new sodium sites due to Na^+ transfer from silicate to carbonate environments. After 10 min of milling two new broad resonances at −10.2 and 2.5 ppm appear in addition to the sharp 16.3 ppm signal (*) of Na_2SiO_3 in the ^{23}Na NMR spectrum due to two new disordered sodium environments. These two peaks slowly merge into one signal at −8.1 ppm after 160 min of milling while no significant change is detected for the resonance at 16.3 ppm. The intensity of the latter drops down sharply after 250 min of milling to be replaced by two sodium signals at −8.0 and 3.5 ppm due to the evolution of a new environment. Complete amorphization is observed after 450 min of grinding (a broad signal at −6.5 ppm with FWHM of 2600 Hz) with only traces of the original sodium environment from sodium metasilicate remaining. This is in harmony with fits to the IR spectra that show a delayed amorphization for the silicate sample.

The amorphization of Na_2CO_3 is also a stepwise process associated with the sites of lower and then of higher symmetry. No changes are visible in the ^{23}Na NMR spectrum during the first 10 min of grinding. A spectrum recorded after 60 min of milling clearly showed a loss of local order for the nine-coordinate sodium. The amorphization of the octahedrally coordinated sodium which is related to broadening of the resonance at ca. 3.8 ppm requires about 150 min of milling. During the
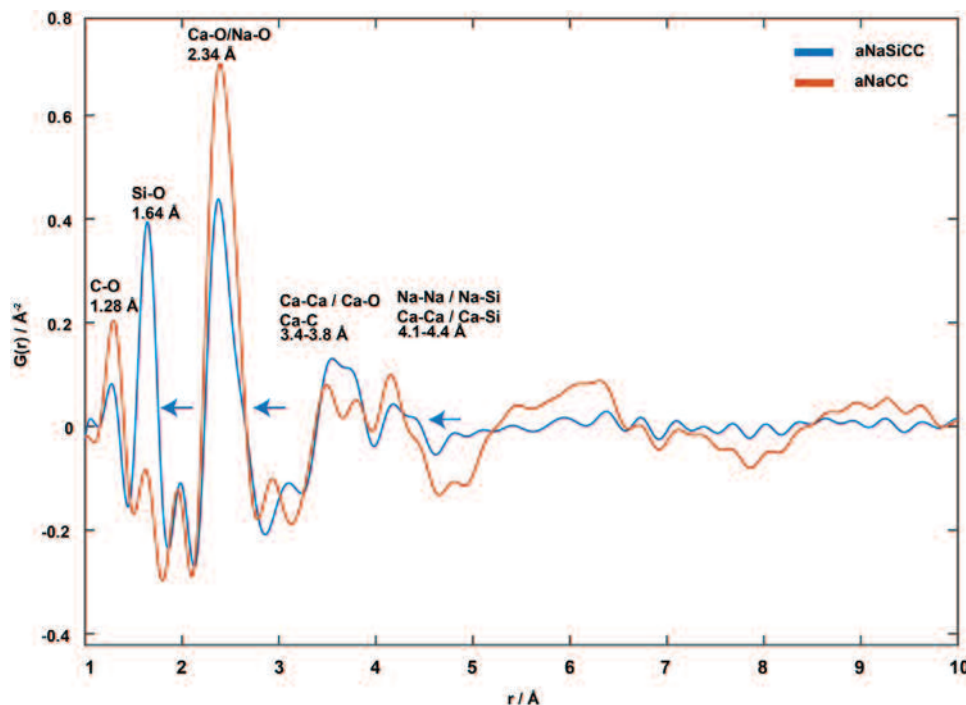
Figure 4. Reduced PDF of aNaSiCC and aNaCC in the range from 1 to 10 Å. Blue arrows mark significant differences between aNaSiCC and aNaCC.

last step two resonances merge into one broad peak with a maximum at −6.5 ppm and an FWHM of 2900 Hz. The comparable FWHM and chemical shifts of the ^{23}Na spectra for aNaSiCC and aNaCC indicate that the amorphization is caused by disorder resulting from the incorporation of sodium cations into the calcium carbonate structure, as ionic radii of Na$^+$ and Ca^{2+} are similar (Ca^{2+}: 1.06 Å; Na$^+$: 0.98 Å).[59]

2.1.3. Structure of aNaCC and aNaSiCC

The short-range order of aNaSiCC and aNaCC was analyzed using X-ray total scattering. The reduced atomic pair distribution function (PDF) G(r) (**Figure 4**) represents the number of atoms in a spherical shell around a reference atom,[60] that is, the absence of any maxima beyond 7 Å is compatible with a non-crystalline structure.[61,62] The termination ripples are due to Fourier termination effects resulting from the finite Q range.[60] While for aNaCC a maximum still appears at 6 Å, the PDF of aNaSiCC fades out after ≈4.3 Å revealing even less structural coherence. A well-defined peak at 1.28 Å corresponds to the C−O separations of the carbonate units. The deviation to the reported C−O distances of 1.25 Å in calcite[52] may be attributed to distortions resulting from the incorporation of different ions and deformation due to milling. The peak at 2.4 Å is associated with non-bonding O-O distances of the carbonate groups and a superposition of first Ca−O and Na−O atom pairs (Figure S1B, D, Supporting Information).[63] The sharp maximum at 1.64 Å in aNaSiCC is associated with typical bond lengths of the tetrahedral SiO$_4$ units,[64] showing the incorporation of silicate groups in the amorphous intermediate. The difference in peak height for the signal at 2.34 Å and a small

shoulder for aNaSiCC at 2.62 Å show different Ca−O and Na−O environments, as no silicate contributions are expected here. More pronounced differences at ≈3.4 and 4.1 Å represent superpositions of several atom pairs, that is, M−M, M−Si, M−C (M = Na, Ca) (Figure S1A, C, Supporting Information). As no sharp maximum appears in the region around 3.1 Å which is associated with interconnected SiO$_4$ units (Figure S1D, Supporting Information)[65] it is assumed that only a broad distribution of Si−O−Si pairs is present in aNaSiCC with no preference for structural order as in crystalline silicates.

2.2. Hydration Reaction

2.2.1. Carbonate Products

The effect of silicate on the reactivity of the sodium-calcium carbonate system was investigated in temperature- and water-induced reactions. Water in acetonitrile mixtures was used to control hydration kinetics by slowing down the reaction and mimic the reaction cascade illustrated in Figure 1.[43,66] Since the hydration rate depends on the water concentration, different water/acetonitrile mixtures were used to simulate the individual reaction steps starting from the amorphous precursors. They are referred to as the first, second, and third hydration steps (corresponding to 5%$_v$, 10%$_v$, and pure water, respectively). Crystallization of aNaCC in a 5%$_v$ H$_2$O/CH$_3$CN mixture led to the formation of pirssonite (Na$_2$Ca(CO$_3$)$_2$ × 2H$_2$O) in an initial step, indicated by a pronounced splitting or broadening of the valence mode of the carbonate group (asymmetric stretch (v_3): 1480 and 1390 cm^{-1}; symmetric stretch (v_1): 1068 cm^{-1}) (**Figure 5**A).[67] Two additional signals at 3210 and 3064 cm^{-1}
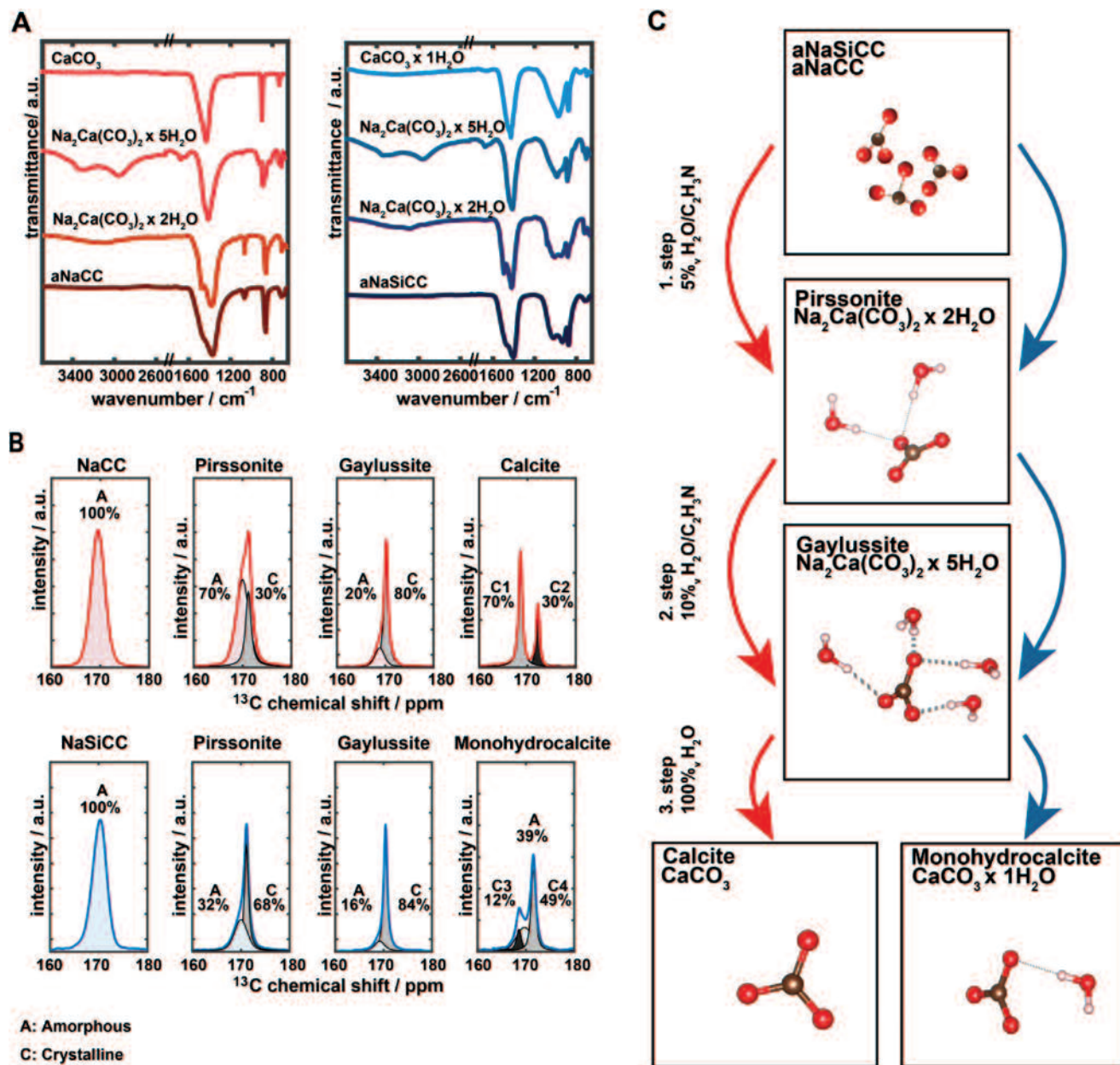
Figure 5. A,B) Evolution of the FTIR and ^{13}C SP MAS-NMR spectra of aNaCC and aNaSiCC upon reaction with H_2O/CH_3CN mixtures. Red spectra represent products obtained from aNaCC, blue spectra correspond to products obtained from aNaSiCC. Kinetic control of the reactions was achieved with variable concentrations of water. Low concentrations (5%$_v$ H_2O/CH_3CN) lead to the formation of pirssonite ($Na_2Ca(CO_3)_2 \times 2H_2O$), intermediate concentrations (10%$_v$ H_2O/CH_3CN) to the formation of gaylussite ($Na_2Ca(CO_3)_2 \times 5H_2O$). High concentrations of water lead to the formation of calcite for aNaCC, whereas monohydrocalcite was formed for NaSiCC. C) Characteristic environments for the carbonate groups in the structures of aNaCC and aNaSiCC:pirssonite, gaylussite, monohydrocalcite, and calcite. The amorphous phases aNaSiCC and aNaCC are assumed to contain a superposition of different carbonate environments with different point symmetries.

show the formation of O-H groups. For intermediate water concentrations (10%$_v$ H_2O/CH_3CN mixture) a sharp signal emerges at 1400 cm^{-1} (v_3 mode), while the band at 1060 cm^{-1} (v_1 mode) vanishes. Additional bands at 3325, 3257, and 2936 cm^{-1} (the regime characteristic for O-H vibrations) are compatible with the formation of gaylussite ($Na_2Ca(CO_3)_2 \times 5H_2O$).[68]

For low and intermediate water concentrations (5%$_v$ and 10%$_v$ H_2O/CH_3CN) the recrystallization of aNaSiCC and aNaCC lead to similar results. However, when the recrystallization

of aNaCC is carried out in an excess of water (or pure water) it proceeds directly to calcite, indicated by a single v_3 band at 1410 cm^{-1} and a pronounced in-plane-deformation band (v_4) at 714 cm^{-1}.[48] In contrast, the reaction of aNaSiCC in pure water leads to a product lacking the v_4 band in the region of 700 cm^{-1}, whose IR spectrum exhibits a slight shoulder at 764 cm^{-1} and a sharp band at 3235 cm^{-1} (characteristic of O-H groups not involved in strong hydrogen bonding). Despite the absence of a characteristic splitting of this v_3 vibration this is compatible

**ADVANCED
SCIENCE NEWS**

www.advancedsciencenews.com

**ADVANCED
FUNCTIONAL
MATERIALS**

www.afm-journal.de

with the formation of monohydrocalcite ($Ca(CO_3) \times H_2O$).[15,48] A magnified view of the IR spectra and a detailed assignment of the infrared modes are given in Figure S2, Table S1, Supporting Information. A detailed analysis of the changes in the silicate environment, based on ^{29}Si NMR and FTIR spectra, is given in the Supporting Information (Figure S3, Table S2, Supporting Information).

Different stages of the reaction were characterized by ^{13}C single pulse- (SP) (Figure 5B) and ^{13}C cross-polarization (CP) MAS NMR spectroscopy (Figures S4–S6, Supporting Information). The single pulse experiments were recorded with a long recycle delay to ensure complete relaxation and to facilitate quantitation. A single broad resonance was observed for aNa-SiCC (chemical shift 170.16 ppm; FWHM 334 Hz) and aNaCC (chemical shift 169.4, FWHM 340 Hz) compatible with a broad distribution of different carbonate environments (vide supra). Incipient hydration led to less symmetric and narrower profiles. According to the results of FTIR and NMR spectroscopy, two different chemical environments are present. The minimum signal approach allows to subdivide the spectra into an amorphous and crystalline part.

A sharp resonance at 171.2 ppm, which was assigned to crystalline pirssonite, appeared in the ^{13}C-NMR spectra of aNaCC (FWHM 134 Hz) and aNaSiCC (98 Hz) during the reaction with 5%$_v$ H_2O/CH_3CN. A signal at 170.4 ppm for aNaCC (FWHM 93Hz) and aNaSiCC (FWHM 83 Hz) was observed for the second reaction step (10%$_v$ H_2O/CH_3CN) corresponding to gaylussite. A sharp resonance at 171.5 ppm (C2, FWHM 114 Hz) for the hydration reaction of aNaSiCC is compatible with the formation of monohydrocalcite[48] for the third reaction step (hydration in pure water), while the sharp resonance for the corresponding reaction of aNaCC at 168.4 ppm (C1, FWHM 81 Hz) is characteristic for calcite. In addition to calcite, a second crystalline environment was found at 172 ppm (C2, FWHM 90 Hz) in aNaCC, which is attributed to Na_2CO_3 (vide infra). A similar behavior was observed in aNaSiCC, where an additional amorphous phase at ≈170 ppm was observed (Figure 5A). A resonance at 168.4 ppm (C3) is attributed to calcite, which is likely to be formed from metastable monohydrocalcite (C4). The evolution of crystalline phases due to hydration was confirmed by powder X-ray diffraction (PXRD) (**Figure 6**).
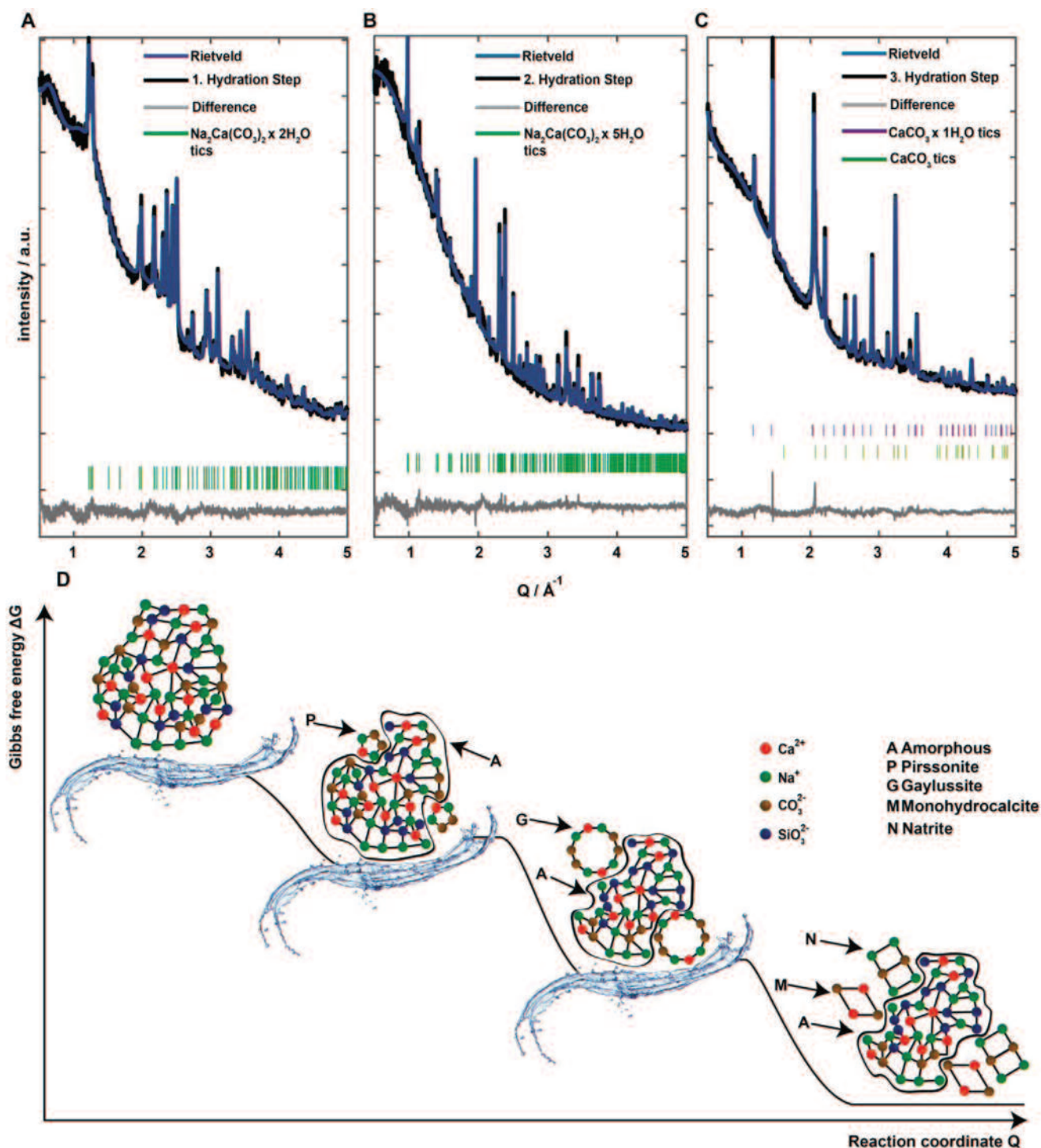
Sharp reflections formed with proceeding hydration (besides an X-ray amorphous background), which fitted none of the typical $CaCO_3$ polymorphs (i.e., vaterite, aragonite, calcite, monohydrocalcite). Pirssonite and gaylussite were identified as reaction products for the hydration of both, aNaCC and aNa-SiCC, by Rietveld refinement.[69] using the TOPAS software package.[70]

It was not possible to index the PXRD data of the last hydration step in aNaSiCC due to a possible multiphasic mixture and broadened reflections. Therefore, 3D electron diffraction (3D ED) was invoked because it allows structural analysis of crystals down to the nanoscale. The 3D reconstruction of the 3D ED data, taken from a nanocrystal with ill-defined morphology (Figure S7, Supporting Information), led to a trigonal unit cell ($a = 6.129(6)$ Å, $c = 7.443(3)$ Å, space group $P3_121/P3_221$, $Z = 3$) of $CaCO_3 \times H_2O$. The relatively thick crystal absorbed almost all of the weak superstructure reflections. Still, it was possible to obtain the first order in section $hk3$ (**Figure 7**). Nevertheless,

by considering the dynamical scattering[71] it was first possible to obtain an inversion twinning and second to identify and refine the hydrogen position of the water molecule ($R_{obs} = 9.87\%$, Table S5, Supporting Information). Thus, it was clearly confirmed that the reflections in the PXRD diffractogram originate from monohydrocalcite[15] and an additional phase identified as natrite (γNa_2CO_3) by FTIR and ^{23}Na MAS NMR (Figures S8–S10, Supporting Information) This allowed to elucidate the reaction pathway outlined in Figure 6D for the hydration reactions of aNaSiCC and aNaCC (Figure S11, Supporting Information).

In summary, an amorphous precursor without long-range order is formed in an "activation step" by ball-milling $CaCO_3$ and soda (Na_2CO_3) or $CaCO_3$ and sodium metasilicate (Na_2SiO_3). The presence of the ionic constituents in "molecular" dispersion allowed for reduced transport distances during crystallization and low activated reactions which are needed for kinetic control in the hydration process. A 100 mg quantity of the intermediates (aNaSiCC or aNaCC respectively) dissolved in 5 mL of a 5%$_v$ water/acetonitrile mixture formally corresponds to a concentration of 400 mg mL^{-1}. Due to the 1:1 ratio of the components in the milling procedure, the average molar masses for aNaSiCC and aNaCC are 222 and 206 g mol^{-1}, respectively. Assuming complete dissolution of aNaSiCC and aNaCC as a first approximation for simplicity, we obtain concentrations in the range of ≈1.9 mol L^{-1} and local ionic strengths in the range of ≈13, that is, the solubility limits would be by far exceeded. Therefore, high local concentrations of Na$^+$, Ca^{2+}, and CO$_3^{2-}$ ions lead to the formation of metastable pirssonite and gaylussite during hydration.[68,72] The hydration reaction starts with the dissolution of aNaSiCC close to the particle surface (**Figure 8**B) and subsequent transport close to crystal surfaces respectively. This leads to high saturation levels of Na$^+$, Ca^{2+} and CO$_3^{2-}$ ions (Figure 8C) and leads to new amorphous and crystalline environments by reversible dissolution/recrystallization processes (Figure 8D), indicated by differences in the proton signals and the relaxation times $T_{1\rho}^H$ in ^{13}C CP experiments due to differences in ^{13}C-^1H separations and ^1H mobility.(Figures S4–S6, S12 and Tables S3 and S4, Supporting Information). The reorganization of the silicate network is assumed to lead to differences observed in the TGA traces of aNaSiCC and aNaCC (Figure S13, Supporting Information). Thermally-induced crystallization of aNaCC and aNaSiCC show the reaction to nyerereite ($Na_2Ca(CO_3)_2$) and Na_2CaSiO_4 (Figure S14, Supporting Information). The emergence of distinct morphologies in close proximity to amorphous domains was observed in TEM (Figure S15, Supporting Information) and SEM (Figure S16, Supporting Information), but ED experiments proved difficult due to the beam sensitivity of the material, showing emerging changes in morphology and diffraction patterns (Figure S17, Supporting Information). For rapid hydration (pure water), gaylussite transformed to calcite (for aNaCC, Figure S18, Supporting Information) or monohydrocalcite (for aNaSiCC, Figure 8E,F). As Na_2CO_3 precipitates despite its high solubility (30.7g Na_2CO_3/100g H_2O) (Figure S8, Supporting Information) it is assumed to leach out after gaylussite formation from small cavities of the product, which hinders dissolution due to confinement (Figures S9 and S10, Supporting Information). Monohydrocalcite forms only from aNaSiCC, while calcite forms from aNaCC. This suggests that

**ADVANCED
SCIENCE NEWS**

www.advancedsciencenews.com

**ADVANCED
FUNCTIONAL
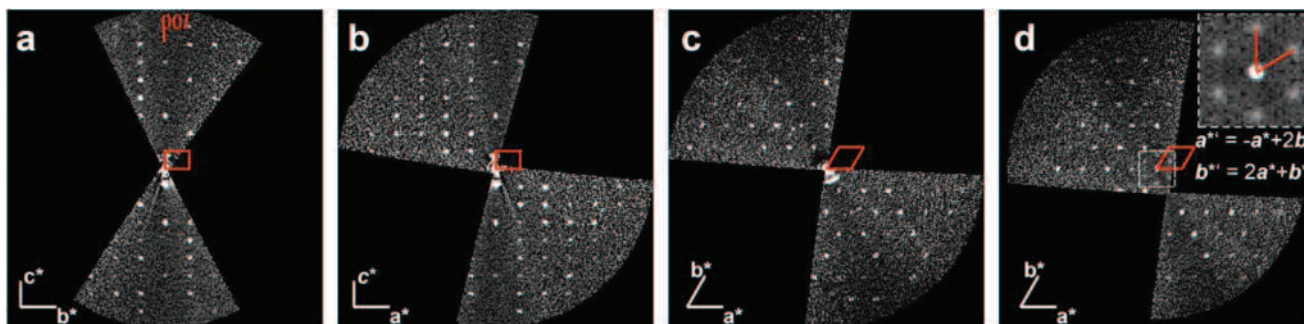MATERIALS**

www.afm-journal.de

Figure 6. X-ray powder diffractograms showing the phase evolution during the hydration reaction of and aNaSiCC prepared by ball-milling. Kinetic control was achieved by lowering the water concentration with CH_3CN. Black lines show the experimental patterns, colored lines the Rietveld refinement. Gray line shows the different patterns, and green ticks indicate the calculated reflection positions of A) pirssonite, B) gaylussite, and C) monohydrocalcite.). D) Schematic energy landscape for the hydration reaction of aNaSiCC via pirssonite and gaylussite to monohydrocalcite and natrite (γ-Na_2CO_3).

the silica environment has a directing effect on recrystallization and, similar to small amounts of foreign ions (Mg^{2+}, PO_4^{3-}) or macromolecules[73] affect polymorph selection of and local order in $CaCO_3$.[74]

In nature, silicate in cystoliths is known to stabilize biogenic ACC.[75] Likewise, silicate has been used synthetically as passive "coating" to stabilize ACC,[34,35] while slow ion diffusion in silica gels,[76,77] and the associated concentration gradients lead

ADVANCED
SCIENCE NEWS
www.advancedsciencenews.com

ADVANCED
FUNCTIONAL
MATERIALS
www.afm-journal.de

Figure 7. Reconstructed sections a–d) 0kl, h0l, 0kl, and 3kl of monohydrocalcite recorded with 3D ED at −176 °C. Weak superstructure reflections in section 3kl are enlarged for clarity.
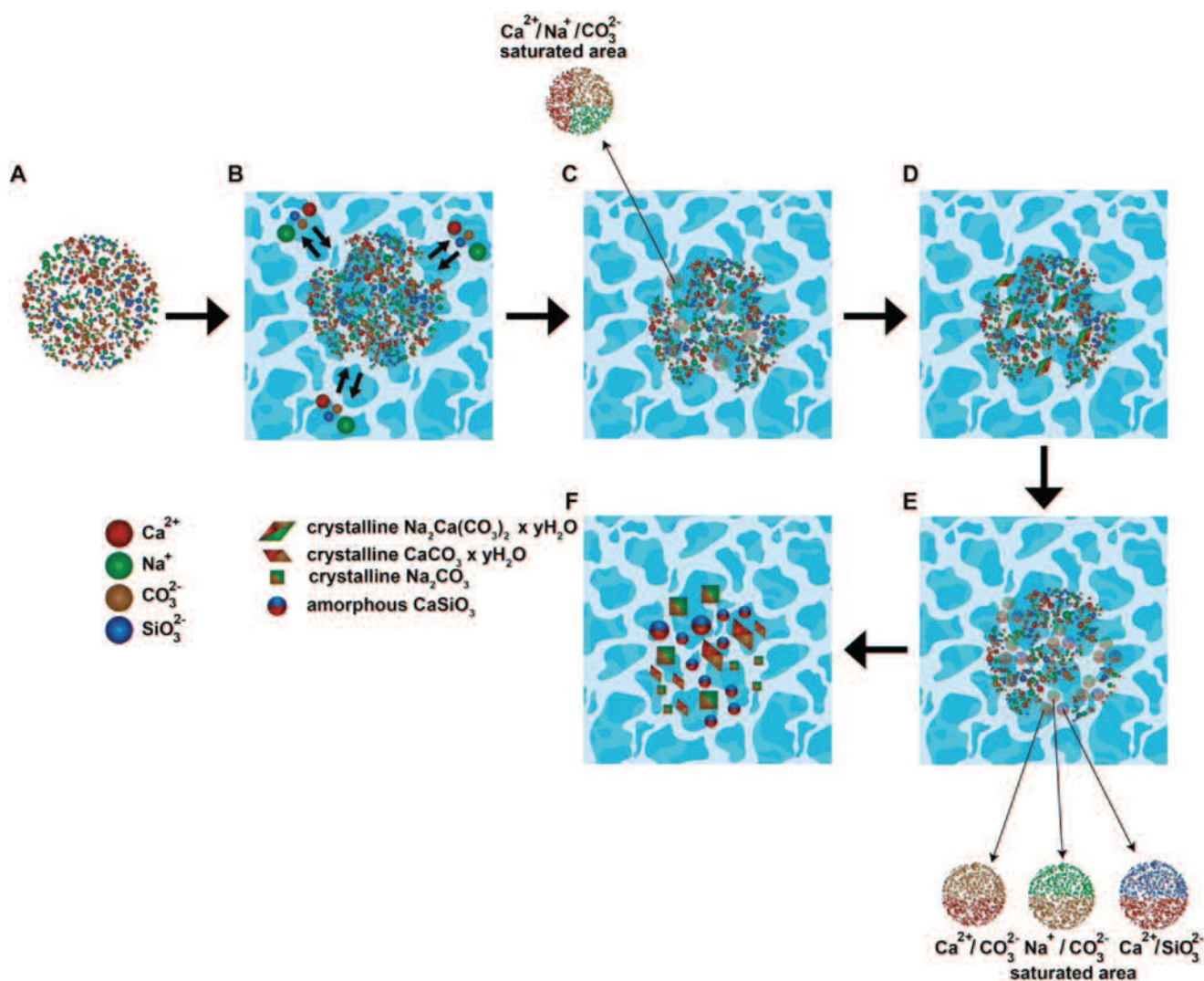
Figure 8. Possible hydration mechanism for aNaSiCC. a) The amorphous activated precursor is brought into contact with a water/acetonitrile mixture. b) Surface dissolution leads to areas of high supersaturation and partial reorganization. c) Crystallization occurs in the areas of high supersaturation. High local concentrations and slow diffusion lead to metastable pirssonite ($Na_2Ca(CO_3)_2 \times 2H_2O$) initially and to gaylussite ($Na_2Ca(CO_3)_2 \times 5H_2O$) for longer reaction times. d) Long contact with water leads to phase separation and formation of areas with high sodium/carbonate, calcium/carbonate, and calcium/silicate concentrations, e) leading to a mixture of Na_2CO_3, $CaCO_3 \times H_2O$ and $Ca,(Na)SiO_3$ nuclei f) eventually transforming to crystalline Na_2CO_3, $CaCO_3 \times H_2O$ and non-crystalline $Ca,(Na)(SiO_3)$.

ADVANCED
SCIENCE NEWS

www.advancedsciencenews.com

ADVANCED
FUNCTIONAL
MATERIALS

www.afm-journal.de

to the formation of monohydrocalcite even in the absence of Mg^{2+} cations. Multi-textured, self-organized monohydrocalcite was formed by temperature-controlled precipitation of $CaCO_3$ in silica.[78] In aNaSiCC, Na^+ and silicate ions are intimately mixed with $CaCO_3$ at a molecular scale. As monohydrocalcite was formed regardless of the hydration reaction, its formation may be related to a retarded crystallization process, similar to a coating of ACC by silicate, associated with the formation of non-crystalline calcium silicates (Figure S3, Supporting Information).

2.2.2. Alkali-Activation of aNaSiCC

aNaCC and aNaSiCC were activated with sodium hydroxide (**Figure 9**).[79] No changes were observed by FTIR for aNaCC (except the formation of small amounts of portlandite), but striking changes occurred in the silicate and carbonate characteristics for aNaSiCC. The decrease of the carbonate/silicate ratio compared to aNaSiCC and the occurrence of a vibration at 953 cm^{-1} which is attributed to a Q2 environment[80] strikingly resembles the C−S−H formation in coprecipitation experiments (Figure 9B).[81] In contrast to aNaSiCC, the X-ray powder diffractogram of the NaOH-activated sample showed reflections at 0.60, 2.06, and 2.26 Å, typical for C−S−H phases (Figure 9C). The reflection at the lowest Q value corresponds to the basal spacing and thus indicates 3D order.[82,83]

Sheet- and fibril-like morphologies as in tobermorite were observed in TEM (Figure 9D).[84,85] The ^{29}Si MAS NMR spectrum showed two sharp resonances at −80.43 (FWHM: 182 Hz) and −85.56 ppm (FWHM: 163 Hz) compatible with Q^1, Q^2, and Q^2b environments.[86,87] due to dreierketten silicate chains (Figure 9E). X-ray total scattering provided additional insight into the short-range order.

A comparison of the reduced PDF between aNaSiCC and NaOH-activated aNaSiCC shows pair correlations in the range of up to 30 Å, indicative of a medium-range order in the C−S−H -like phase (Figure 9F). Similar to aNaSiCC, the maxima at 1.2, 1.6, and 2.4 Å correspond to C−O, Si−O, and M−O pairs,[88] where the C−O distance shows a slight shift to lower r values. Differences in peak profiles and intensities are linked to differences in the short-range order, that is, the atom coordination numbers. In contrast to the amorphous aNaSiCC, a peak now occurs at 3.1 Å that correlates with a Si−Si pair, which can be attributed to Si−Si separations associated with the corner-sharing tetrahedra in the Dreierketten silicate structure.

A comparison of aNaSiCC, as a starting material to CSH, with a reference of amorphous calcium silicate (aCS, Figure S19, Supporting Information) before and after activation shows similar PDFs for the starting materials, as well as the obtained C−S−H phases. A distinct difference is the pronounced pair-pair distance at 1.28 Å resulting from the included carbonate groups in aNaSiCC and alkali-activated aNaSiCC. The sharp peak at 3.72 Å is attributed to the Ca−Si pair from the silica chain, which is adjacent to the central Ca−O layer. This separation becomes smaller in carbonated C−S−H, which was attributed to decalcification.[89] The material described here does not show such a behavior, although being carbonate-rich. This implies a new pathway to a C−S−H-like
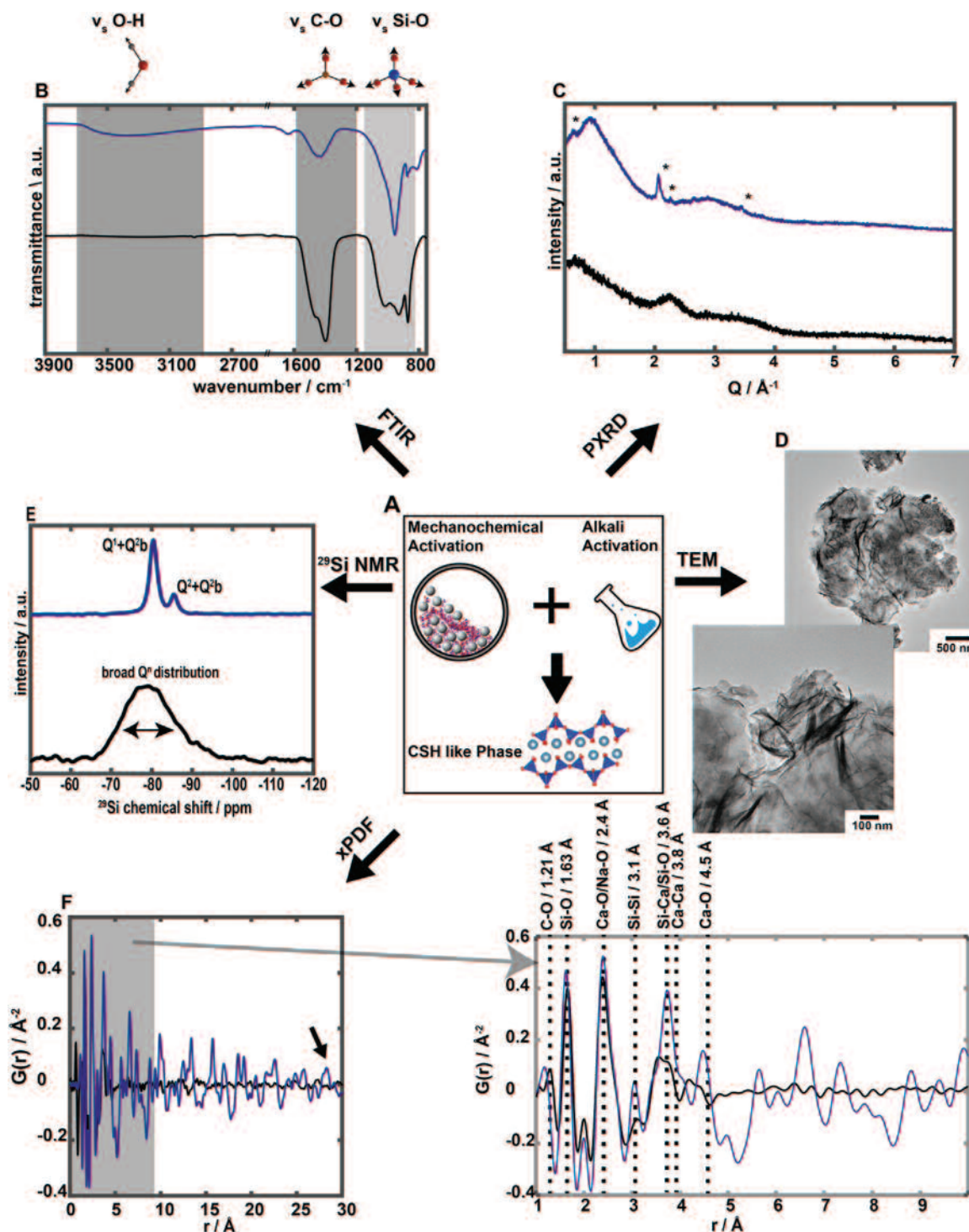
material by mechanochemical activation without preceding calcination of the calcium source. A previous study has shown that the activation of calcium carbonate with sodium silicate solutions leads to a mixture of C−S−H with high contents of crystalline calcium carbonates results from a variety of dissolution and recrystallization processes.[7] The mechanochemical approach allows a new chemical approach, which is due to the different arrangement of the "molecular" building blocks in the activated amorphous precursor phase.

3. Conclusion

Making alternative binders from available and cheap natural raw materials such as calcium carbonate or geopolymers/alkali-activated binders is an environmentally friendly solution for the sustainable development of building materials. Many natural raw materials contain several mineral phases often including calcium carbonates which define their reactivity. We have studied the salt metathesis reaction of calcium carbonate ($CaCO_3$) with solid sodium silicate (Na_2SiO_3) and its role in geopolymer/alkali-activated binders. High-temperature treatment and the associated CO_2 emissions can be avoided by a grinding activation step. The formation of the cement paste and the hydration reactions proceed via a complex cascade of non-equilibrium reactions before reaching thermodynamic equilibrium. An amorphous intermediate (aNaSiCC) of $CaCO_3$ and Na_2SiO_3 containing the ionic constituents in "molecular" dispersion is prepared in the ball-milling activation step. This allows for molecular transport pathways during hydration reactions and extremely low activated reactions, because the precipitation of solids from liquids, which is nucleation limited and kinetically controlled, and solid-state transformations, which are diffusion-limited and thermodynamically controlled, have almost equal weighting. Elementary steps of the hydration reaction could be resolved by a combination of FTIR and multinuclear MAS-NMR spectroscopy with automated ED tomography.

Ball milling typically leads to reactive defect-rich structures with poorly defined crystal domains that elude structural analysis using conventional diffraction methods. We show here that despite the challenges in the structure analysis of poorly crystalline nanomaterials, even fine structural details can be elucidated with 3D ED.

A multistep cascade of hydration reactions occurs starting from the amorphous aNaSiCC precursor via pirssonite ($Na_2Ca(CO_3)_2$ x $2H_2O$) and gaylussite ($Na_2Ca(CO_3)_2$ x $5H_2O$) to monohydrocalcite. Activation of aNaSiCC with a NaOH leads to a phase with structural similarity to C−S−H. The formation of pirssonite and gaylussite suggests that alkali metals are removed from the binder in water and promote the formation of a C−S−H phase containing some sodium. The used C/S ratio of ≈ 1 is compatible with a defect tobermorite structure. Our results outline a possibility for cement production without CO_2 emissions at ambient temperature. High-temperature treatment and the associated CO_2 emissions can be circumvented by a simple grinding activation step. Since grinding is a standard technique in the cement industry, an industrial scale implementation may be feasible. The electrical energy consumption in our experiments requires ≈120 kWh (or ≈0.43 GJ) per ton of

Figure 9. Preparation of the activated precursor aNaSiCC and structural characterization of aNaSiCC and NaOH-activated products. A) Mechano-chemical activation of $CaCO_3/Na_2CO_3$ and $CaCO_3/Na_2SiO_3$ mixtures by ball milling and chemical activation with sodium hydroxide. B) FTIR spectra of aNaSiCC (black line) and NaOH-activated product (blue line). C) X-ray powder diffractograms of aNaSiCC (black line) and NaOH-activated product (blue line) showing the virtually amorphous structure of the activated aNaSiCC precursor. The reflections at 0.60, 2.06, and 2.26 $Å^{-1}$ for the NaOH-activated product are typical for C−S−H phases. The reflection at 0.60 $Å^{-1}$ corresponds to the basal C−S−H spacing and indicates 3D order. D) TEM image of NaOH-activated aNaSiCC with foil-like and fibrillary morphologies. E) ^{29}Si MAS NMR spectra of aNaSiCC (black line) and NaOH-activated product (blue line) with two sharp resonances at −80.43 (FWHM: 182 Hz) and −85.56 ppm (FWHM: 163 Hz) indicating Q^1, Q^2, and Q^2b environments due to dreierketten silicate chains. The spectrum of aNaSiCC (black line) shows only one broad signal due to disorder. F) Reduced pair distribution functions of aNaSiCC (black line) and NaOH-activated aNaSiCC (blue line). The PDF of aNaSiCC fades out beyond 4 Å. The NaOH-activated product shows pronounced signals up to 30 Å compatible with a C−S−H related structure having distinct silicate environments and medium-range order.

**ADVANCED
SCIENCE NEWS**
www.advancedsciencenews.com

**ADVANCED
FUNCTIONAL
MATERIALS**
www.afm-journal.de

cement, while the specific thermal energy in clinker production is reported to be 4–5 GJ t^{-1}.[1–3] Thus, the energy savings of the non-optimized laboratory test compared to an energy-optimized manufacturing process roughly corresponds to a factor of 10 (i.e., one order of magnitude). Still, this energy conservation corresponds only to the CO_2 emission by fossil fuel combustion during cement production. Limestone can be prepared by directly dissolving CO_2 from flue gas in water in a pressure separation plant followed by injection for mineral storage.[90]

Additionally, CO_2 is a by-product of the chemical conversion process during clinker production, where limestone ($CaCO_3$) is converted to lime (CaO). Since no CO_2 is released in the milling process leading to the formation of aNaSiCC, our approach may circumvent a massive release of CO_2, corresponding to a CO_2 saving on a gigaton scale worldwide. Although these rough estimates cannot be compared to an industrial process, where development, design, feasibility, maintenance, and other parameters must be considered, our approach may open up a route to dramatically reduce CO_2 emissions in cement production.

4. Experimental Section

Materials: Calcite (98%, Socal 31, Solvay), sodium carbonate (anhydrous 99.5%, Alfa Aesar), calcium carbonate-^{13}C (99 atom % ^{13}C, isotec), sodium metasilicate (≈18 mesh, Alfa Aesar), cyclohexane (analytical reagent grade, Fisher Chemicals), calcium hydroxide (95%, Alfa Aesar), silica fumed powder (0.007 µm, Sigma Aldrich), ethanol (absolute 99.8+%, Fisher Chemicals), acetonitrile (for HPLC, gradient grade, 99.9%, Honeywell Riedel-de Haën), and doubly-deionized water (resistivity > 18mΩ cm).

Synthesis of Amorphous Sodium Calcium Carbonate (aNaSiCC): Sodium carbonate (0.257 g, 2.4 mmol) was treated with calcium carbonate (0.243 l g, 2.4 mmol) in a planetary ball mill (Pulverisette 7 Classic, Fritsch). The starting materials and 9 mL of cyclohexane were transferred together with 7.5 grams of grinding balls (about 2000 balls, 1 mm diameter, ZrO_2) into ZrO_2 grinding jars. The mixture was milled for 15 h at 720 rpm. To avoid overheating, alternate 10 min of grinding and then a 10 min rest phase was used. Therefore, 450 min of ball milling results in a reaction time of 900 min. Afterward, the cyclohexane was removed with a pipette. The product was dispersed in ethanol, separated from the grinding balls by decantation, then isolated by centrifugation, and dried in vacuo.

Synthesis of Amorphous Sodium Silicate Calcium Carbonate (aNaCC): Sodium metasilicate (0.243 g, 2.29 mmol) was treated with calcium carbonate (0.257 l g, 2.57 mmol) in a planetary ball mill (Pulverisette 7 Classic, Fritsch). The starting materials and 10 mL of cyclohexane were transferred together with 3.65 grams of grinding balls (about 1100 balls, 1 mm diameter, ZrO_2) into ZrO_2 grinding jars. The mixture was milled for 15 h at 720 rpm. To avoid overheating, intermittent grinding (10 min of grinding /10 min rest phase) was used. Therefore, 450 min of ball milling corresponds to a reaction time of 900 min. Cyclohexane was removed with a pipette after the reaction. The product was dispersed in ethanol, separated from the grinding balls by decantation, then isolated by centrifugation, and dried in vacuo.

Synthesis of Amorphous Calcium Silicate (aCS): Calcium hydroxide (0.277g, 3.7 mmol) was treated with fumed silica powder (0.233g, 3.7 mmol) in a planetary ball mill. (Pulverisette 7 Classic, Fritsch). The starting materials and 9 mL of cyclohexane were transferred together with 7.5 grams of grinding balls (about 2000 balls, 1 mm diameter, ZrO_2) into ZrO_2 grinding jars. The mixture was milled for 3 h at 720 rpm. To avoid overheating, alternate 10 min of grinding and then a 10 min rest phase was used. Therefore, 180 min of ball milling results in a reaction time of 360 min. Afterward, the cyclohexane was removed with a pipette. The product was dispersed in ethanol, separated from the

grinding balls by decantation, then isolated by centrifugation, and dried in vacuo.

Crystallization Experiments: Crystallization experiments were carried out by adding 100 mg of aNaSiCC or aNaCC to solutions of 5%v or 10%v acetonitrile in water or pure water (resulting in concentrations of 20 mg mL^{-1}). To monitor crystallization ex situ at a given time 1 mL of the dispersion was transferred to a microreaction vessel containing 0.5 mL of acetone. After centrifugation, the liquid phase was decanted, washed with acetone again, and dried in vacuo.

X-Ray Powder Diffraction: X-ray diffractograms were recorded with a STOE Stadi P equipped with a Mython 1k detector using Mo Kα_1 radiation ($\lambda = 0.7093$ Å). The dry samples were prepared between polyvinyl acetate foils in perfluoroether (Fomblin Y, Aldrich). The measurements were performed in the 2θ range from 2° to 45° with a step size of 0.015° (continuous scan, 150 s deg^{-1}). Crystalline phases were identified with the PDF-2 database using Bruker AXS.

ATR-FTIR Spectroscopy: Attenuated total reflection (ATR) FTIR spectra were recorded on a Nicolet iS10 spectrometer (Thermo scientific) in the frequency range from 550 to 4000 cm^{-1} with a resolution of 1.4 cm^{-1} per data point.

Solid-State NMR Spectroscopy: All solid-state NMR spectra were recorded on a Bruker Advance 400 DSX NMR spectrometer (Bruker BioSpin GmbH, Rheinstteten, Germany operated by Topspin 1.3, 2007, patchlevel 8) at a ^{1}H frequency of 399.87 MHz, ^{13}C frequency of 100.55 MHz, and ^{31}P frequency of 161.87 MHz. A commercial 3 channel 4 mm Bruker probe head at 10 kHz MAS was used for all experiments. The ^{1}H NMR spectra and ^{1}H background-corrected spectra were recorded averaging 32 transients with 8 s recycle delay. For all solid-state ^{13}C CP MAS NMR experiments, an initial 90° pulse with 4.0 µs length and 5 s recycle delay were used. A ramped CP pulse (from 64 to 100%) with duration of 20 µs, 50 µs, 100 µs, 200 µs, 500 µs, 1 ms, 2 ms, 3 ms, 5 ms, and 7 ms was used for recording the CP build-up curves. Two pulse phase modulation (TPPM) ^{1}H decoupling scheme was used while acquiring the ^{13}C signal. 512 transients were averaged for the CP experiments. The spectra were baseline-corrected, and a broadening of 60 Hz was applied. Quantitative ^{13}C single pulse excitation experiments allowing full relaxation were recorded by averaging 16 transients with a recycle delay of 2200 s and TPPM heteronuclear decoupling. Spectral deconvolution was performed using self-written MatLab scripts (version 2017b).

Thermal Analysis: Coupled thermogravimetry-differential thermal analysis (TG-DTA) was carried out on a Netzsch STA 449 F3 Jupiter device. About 10 mg of the sample was heated in an alumina cup in argon atmosphere from 50 to 650 °C at a heating rate of 10 K min^{-1}.

Transmission Electron Microscopy (TEM): Imaging and simple diffraction measurements were acquired on an FEI Tecnai G2 Spirit microscope operating at 120 kV (LaB$_6$ filament), equipped with a Gatan US1000 CCD-camera (16-bit, 2048×2048 pixels). Samples were prepared by placing one drop (15 µL) of a diluted nanoparticle dispersion in ethanol on a carbon-coated copper grid and letting it dry at room temperature. 3D ED measurement of monohydrocalcite was carried out with a TEM FEI Tecnai F30 S-TWIN equipped with a field emission gun (300 kV). The powdered sample was dispersed in ethanol using an ultrasonic bath and sprayed on carbon-coated copper grid using an ultrasound sonifier[91] TEM images and EDED patterns were acquired with a Gatan UltraScan4000 CCD camera (16-bit, 4096×4096 pixel) at hardware-binning of 4. Scanning transmission electron microscopy (STEM) images were collected by a FISCHIONE high-angular annular dark field (HAADF) detector and acquired by Emispec ES Vision software. 3D ED data were collected using the acquisition module Fast-ADT (FADT) developed for FEI and JEOL microscopes.[92] A condenser aperture of 10 µm and mild illumination settings (gun lens 8, spot size 6) were used in order to produce a semi-parallel beam of 520 nm in diameter (0.12 e^{-} Å^{-2} s^{-1}). Crystal position tracking was performed in microprobe STEM mode. For tilt experiments acquisitions were performed with a Gatan cryo-transfer tomography holder. Prior to the measurements the sample and the stage were cooled under cryogenic conditions. The ED data were collected on both TEMs with electron beam precession (precession ED, PED) to improve reflection intensity integration quality.[93,94] PED was performed

using a Digistar unit developed by NanoMEGAS SPRL. The precession angle was kept at 1.0°. The PETS2.0 software package was used for 3D ED data processing.[95] Difference Fourier mapping and least-squares (dynamical) refinement were performed with the software JANA2006.[96] U_{iso} of the atomic sites C1, O1, O2, and O3 were kept to be the same.

X-Ray Total Scattering for Pair Distribution Function Analysis: To obtain structural information about the short-range order X-ray total scattering for PDF analysis was performed with data acquired from Beamline 11-ID-B of the Advanced Photon Source (APS, Argonne, Il). An incident photon energy of 58.6 keV ($\lambda = 0.2115$ Å) was used, and the samples were measured in transmission through a 3 mm polyimide (Kapton) capillary with a sample-to-detector distance of 158 mm. The scattering patterns were measured using an amorphous Si Perkin Elmer detector system (2048×2048 pixels, 200 × 200 μm^2 pixel size). To calibrate the sample-to-detector distance, tilt and pitch relative to the incident beam path a CeO_2 standard was used for calibration. The obtained 2D scattering data was integrated from 0.5 to 24 Å^{-1} in GSAS-II to produce on-dimensional scattering profiles.[97] PDFgetX3 was used to process the experimental total scattering data.[98]

Corrections such as background subtraction (by measuring the empty Kapton tube), contributions from incoherent scattering, and corrections for nonlinear detector efficiency or normalization by the average atomic scattering cross-section of the sample were applied using this software. The stoichiometric compositions of the amorphous materials, $Na_2Ca(CO_3)_2$ in aNaCC and $Na_2Ca(SiO_3)(CO_3)$ in aNaSiCC, were used for data normalization.

Supporting Information

Supporting Information is available from the Wiley Online Library or from the author.

Acknowledgements

Conflict of Interest

The authors declare no conflict of interest.

Author Contributions

M.M.: Synthesis, characterization, writing, total scattering – original draft. T.G.: Synthesis. G.M.: Automated electron diffraction tomography. P.O.: Total scattering. M.M.: Nuclear magnetic resonance spectroscopy. Y.K.: Automated electron diffraction tomography. U.K.: Electron microscopy, Resources. W.T.: Conceptualization, Writing – review and editing, Supervision, Project administration, Funding acquisition.

Data Availability Statement

Research data are not shared.

[1] R. Andrew, *Earth Syst. Sci. Data* **2018**, *10*, 195.
[2] E. Gartner, H. Hirao, *Cem. Concr. Res.* **2015**, *78*, 126.
[3] J. L. Provis, *Cem. Concr. Res.* **2018**, *114*, 40.
[4] X. Ouyang, D. A. Koleva, G. Ye, K. v. Breugel, *Mater. Struct.* **2017**, *50*, 213.
[5] H. Niu, M. Abdulkareem, H. Sreenivasan, A. M. Kantola, J. Havukainen, M. Horttanaien, V.-V. Telkki, P. Kinnunen, M. Illikainen, *Miner. Eng.* **2020**, *157*, 106535.
[6] D. E. Ortega-Zavala, J. L. Santana-Carrillo, O. Burciaga-Díaz, J. I. Escalante-García, *Cem. Concr. Res.* **2019**, *120*, 267.
[7] R. Firdous, T. Hirsch, D. Klimm, B. Lothenbach, D. Stephan, *Miner. Eng.* **2021**, *165*, 106849.
[8] W. A. Gutteridge, J. A. Dalziel, *Cem. Concr. Res.* **1990**, *20*, 778.
[9] M. Cyr, P. Lawrence, E. Ringot, *Cem. Concr. Res.* **2005**, *35*, 719.
[10] E. Berodier, K. Scrivener, *J. Am. Ceram. Soc.* **2014**, *97*, 3764.
[11] T. Matschei, B. Lothenbach, F. P. Glasser, *Cem. Concr. Res.* **2007**, *37*, 551.
[12] F. C. Meldrum, *Int. Mater. Rev.* **2003**, *48*, 187.
[13] J. W. Morse, R. S. Arvidson, A. Lüttge, *Chem. Rev.* **2007**, *107*, 342.
[14] K.-F. Hesse, H. Küppers, *Z. Kristallogr. Cryst. Mater.* **1983**, *163*, 227.
[15] H. Effenberger, *Monatsh. Chem.* **1981**, *112*, 899.
[16] Z. Zou, W. J. E. M. Habraken, G. Matveeva, A. C. S. Jensen, L. Bertinetti, M. A. Hood, C.-Y. Sun, P. U. P. A. Gilbert, I. Polishchuk, B. Pokroy, J. Mahamid, Y. Pliti, S. Weiner, P. Werner, S. Bette, R. Dinnebier, U. Kolb, E. Zolotoyabko, P. Fratzl, *Science* **2019**, *363*, 396.
[17] L. Addadi, S. Raz, S. Weiner, *Adv. Mater.* **2003**, *15*, 959.
[18] D. Gebauer, M. Kellermeier, J. D. Gale, L. Bergström, H. Cölfen, *Chem. Soc. Rev.* **2014**, *43*, 2348.
[19] J. J. D. Yoreo, P. U. P. A. Gilbert, N. A. J. M. Sommerdijk, R. L. Penn, S. Whitelam, D. Joester, H. Zhang, J. D. Rimer, A. Navrotsky, J. F. Banfield, A. F. Wallace, F. M. Michel, F. C. Meldrum, H. Cölfen, P. M. Dove, *Science* **2015**, *349*, aaa6760 .
[20] N. T. K. Thanh, N. Maclean, S. Mahiddine, *Chem. Rev.* **2014**, *114*, 7610.
[21] J. Lee, J. Yang, S. G. Kwon, T. Hyeon, *Nat. Rev. Mater.* **2016**, *1*, 16034.
[22] L. B. Gower, D. J. Odom, *J. Cryst. Growth* **2010**, *4*, 719.
[23] D. Gebauer, A. Völkel, H. Cölfen, *Science* **2008**, *322*, 1819.
[24] S. E. Wolf, J. Leiterer, M. Kappl, F. Emmerling, W. Tremel, *J. Am. Chem. Soc.* **2008**, *130*, 12342.
[25] S. E. Wolf, J. Leiterer, V. Pipich, R. Barrea, F. Emmerling, W. Tremel, *J. Am. Chem. Soc.* **2011**, *133*, 12642.
[26] Y. U. T. Gong, C. E. Killian, I. C. Olson, N. P. Appathurai, A. L. Amasino, M. C. Martin, L. J. Holt, F. H. Wilt, P. U. P. A. Gilbert, *Proc. Natl. Acad. Sci. U. S. A.* **2012**, *109*, 6088.
[27] D. J. Tobler, J. D. Rodriguez-Blanco, K. Dideriksen, N. Bovet, K. K. Sand, S. L. S. Stipp, *Adv. Funct. Mater.* **2015**, *25*, 3081.
[28] C. Günther, A. Becker, G. Wolf, M. Epple, *Z. Anorg. Allg. Chem.* **2005**, *631*, 2830.
[29] D. Pontoni, J. Bolze, N. Dingenouts, T. Narayanan, M. Ballauff, *J. Phys. Chem. B* **2003**, *107*, 5123.
[30] J.-D. Rodriguez-Blanco, S. Shaw, L. G. Benning, *Nanoscale* **2011**, *3*, 265.
[31] P. Bots, L. G. Benning, J.-D. Rodriguez-Blanco, T. Roncal-Herrero, S. Shaw, *Cryst. Growth Des.* **2012**, *12*, 3806.

[32] M. Dietzsch, I. Andrusenko, R. Branscheid, F. Emmerling, U. Kolb, W. Tremel, *Z. Kristallogr. Cryst. Mater.* **2016**, *232*, 255.

[33] M. Kellermeier, D. Gebauer, E. Melero-García, M. Drechsler, Y. Talon, L. Kienie, H. Cölfen, J. M. García-Ruiz, W. Kunz, *Adv. Funct. Mater.* **2012**, *22*, 4301.

[34] J. Ihli, W. C. Wong, E. H. Noel, Y.-Y. Kim, A. N. Kulark, H. K. Christenson, M. J. Duer, F. C. Meldrum, *Nat. Commun.* **2014**, *5*, 3169.

[35] M. Kellermeier, E. Melero-Garcia, F. Glaab, R. Klein, M. Drechsler, R. Rachel, J. M. Garcia-Ruiz, W. Kunz, *J. Am. Chem. Soc.* **2010**, *132*, 17859.

[36] S. Sjöberg, *J. Non-Cryst. Solids* **1996**, *196*, 51.

[37] M. Kellermeier, F. Glaab, R. Klein, E. Melero-García, W. Kunz, J. M. García-Ruiz, *Nanoscale* **2013**, *5*, 7054.

[38] H. Schäfer, *Angew. Chem., Int. Ed.* **1971**, *10*, 43.

[39] A. Stein, S. W. Keller, T. E. Mallouk, *Science* **1993**, *259*, 1558.

[40] S. Leukel, M. Panthöfer, M. Mondeshki, G. Kieslich, Y. Wu, N. Krautwurst, W. Tremel, *Chem. Mater* **2018**, *30*, 6040.

[41] P. Opitz, M. P. Asta, A. Fernandez-Martinez, M. Panthöfer, A. Kabelitz, F. Emmerling, M. Mondeshki, W. Tremel, *Cryst. Growth Des.* **2020**, *10*, 6831.

[42] S. R. Bauers, S. R. Wood, K. M. Ø. Jensen, A. B. Blichfeld, B. B. Iversen, S. J. L. Billinge, D. C. Johnson, *J. Am. Chem. Soc.* **2015**, *137*, 9652.

[43] S. Leukel, W. Tremel, *Cryst. Growth Des.* **2018**, *18*, 4662.

[44] S. Kirkpatrick, C. D. GelattJr., M. P. Vecchi, *Science* **1983**, *220*, 671.

[45] D. A. Kulik, *Cem. Concr. Res.* **2011**, *41*, 477.

[46] I. G. Richardson, *Cem. Concr. Res.* **2008**, *38*, 137.

[47] L. Zedler, M. Hager, U. Schubert, M. J. Harrington, M. Schmitt, J. Popp, B. Dietzek, *Mater. Today* **2014**, *17*, 57.

[48] H. Nebel, M. Neumann, C. Mayer, M. Epple, *Inorg. Chem.* **2008**, *47*, 7874.

[49] H. Liu, S. Ho Hahn, M. Ren, M. Thiruvillamalai, T. M. Gross, J. Du, A. C. T. v. Duin, S. H. Kim, *J. Am. Ceram. Soc.* **2020**, *103*, 3575.

[50] E. Dowty, *Phys. Chem. Miner.* **1987**, *14*, 80.

[51] H. Eckert, *J. Sol-Gel Sci. Technol.* **2018**, *88*, 263.

[52] H. Sitepu, B. H. O'Connor, D. Li, *J. Appl. Crystallogr.* **2005**, *38*, 158.

[53] Ž. Čančarević, J. C. Schön, M. Jansen, *Z. Anorg. Allg. Chem.* **2006**, *632*, 1437.

[54] A. R. Jones, R. Winter, G. N. Greaves, I. H. Smith, *J. Phys. Chem. B* **2005**, *49*, 23154.

[55] H. Koller, G. Engelhardt, A. O. M. Kentgens, J. Sauer, *J. Phys. Chem.* **2002**, *6*, 1544.

[56] W. S. McDonald, D. W. J. Crucikshank, *Acta Crystallogr.* **1967**, *22*, 37.

[57] M. Dusek, G. Chapuis, M. Meyer, V. Petricek, *Acta Crystallogr., Sect. B: Struct. Sci., Cryst. Eng. Mater.* **2003**, *B59*, 337.

[58] A. M. George, S. Sen, J. F. Stebbins, *Solid State Nucl. Magn. Reson.* **1997**, *10*, 9.

[59] V. M. Goldschmidt, *Naturwissenschaften* **1926**, *14*, 477.

[60] T. Egami, S. J. Billinge, *Underneath the Bragg Peaks*, Pergamon, London **2003**.

[61] H.-W. Wang, L. L. Daemen, M. C. Cheshire, M. K. Kidder, A. G. Stack, L. F. Allard, J. Neuefeind, D. Olds, J. Liu, K. Page, *Chem. Commun.* **2017**, *20*, 2942.

[62] J. Huang, J. D. Blakemore, D. Fazi, O. Kokhan, N. D. Schley, R. H. Crabtree, G. W. Brudvig, D. M. Tiede, *Phys. Chem. Chem. Phys.* **2014**, *5*, 1814.

[63] H.-W. Wang, L. L. Daemen, M. C. Cheshire, M. K. Kidder, A. G. Stack, L. F. Allard, J. Neuefeind, D. Olds, J. Lie, K. Page, *Chem. Commun.* **2017**, *20*, 2942.

[64] M. G. Tucker, M. T. Dove, D. A. Keen, *J. Phys.: Condens. Matter* **2000**, *12*, 425.

[65] S. Bae, H. Jee, H. Suh, M. Kanematsu, A. Shiro, A. Machida, T. Watanuki, S. Morooka, G. Geng, H. Suzuki, *Constr. Build. Mater.* **2020**, *237*, 117714.

[66] F. Manoli, E. Dalas, *J. Cryst. Growth* **2000**, *218*, 359.

[67] H. H. Adler, P. F. Kerr, *Am. Mineral.* **1963**, *48*, 839.

[68] C. R. Bury, R. Redd, *J. Chem. Soc.* **1933**, 1160.

[69] H. M. Rietveld, *Z. Kristallogr. Cryst. Mater.* **2010**, *12*, 545.

[70] A. A. Coelho, *J. Appl. Crystallogr.* **2018**, *51*, 210.

[71] L. Palatinus, P. Brázda, P. Boullay, O. Perez, M. Klementová, S. Petit, V. Eigner, M. Zaarour, S. Mintova, *Science* **2017**, *355*, 166.

[72] F. E. Littman, H. J. Gaspari, *Ind. Eng. Chem.* **1956**, *48*, 408.

[73] M. Balz, H. A. Therese, J. Li, J. S. Gutmann, M. Kappl, L. Nasdala, W. Hofmeister, H.-J. Butt, W. Tremel, *Adv. Funct. Mater.* **2005**, *15*, 683.

[74] F. Natalio, T. Coralles, M. Panthöfer, I. Lieberwirth, D. Schollmeyer, W. E. G. Müller, M. Kappl, H.-J. Butt, W. Tremel, *Science* **2013**, *339*, 1298.

[75] A. Gal, S. Weiner, L. Addadi, *J. Am. Chem. Soc.* **2010**, *132*, 13208.

[76] G. Zhang, J. M. Delgado-López, D. Choquesillo-Lazarte, J. M. García-Ruiz, *CrystEngComm* **2013**, *15*, 6526.

[77] J. W. McCauley, R. Roy, *Am. Mineral.* **1974**, *59*, 947.

[78] G. Zhang, C. Verdugo-Escamilla, D. Choquesillo-Lazarte, J. M. García-Ruiz, *Nat. Commun.* **2018**, *9*, 5221.

[79] F. Pacheco-Torgal, J. Castro-Gomes, S. Jalali, *Constr. Build. Mater.* **2008**, *22*, 1315.

[80] P. Yu, R. J. Kirkpatrick, B. Poe, P. F. McMilan, X. Cong, *J. Am. Ceram. Soc.* **1999**, *82*, 742.

[81] S. Steiner, B. Lothenbach, T. Proske, A. Borgschulte, F. Winnefeld, *Cem. Concr. Res.* **2020**, *135*, 106116.

[82] E. T. Rodriguez, K. Garbev, D. Merz, L. Black, I. G. Richardson, *Cem. Concr. Res.* **2017**, *93*, 45.

[83] K. Garbev, G. Beuchle, M. Bornefeld, L. Black, P. Stemmermann, *J. Am. Ceram. Soc.* **2008**, *91*, 3005.

[84] I. G. Richardson, *Cem. Concr. Res.* **2004**, *34*, 1733.

[85] H. Li, T. Du, H. Xiao, Q. Zhang, *J. Am. Ceram. Soc.* **2017**, *100*, 3227.

[86] X. Cong, J. Kirkpatrick, *Adv. Cem. Based Mater.* **1996**, *3*, 144.

[87] I. G. Richardson, J. Skibstedt, L. Black, R. J. Kirkpatrick, *Adv. Cem. Res.* **2010**, *22*, 233.

[88] S. Grangeon, A. Fernandez-Martinez, A. Baronnet, N. Marty, A. Poulain, E. Elkaïm, C. Roosz, G. P. Henocq, F. Claret, *J. Appl. Crystallogr.* **2017**, *50*, 14.

[89] A. E. Morandeau, C. E. White, *J. Mater. Chem. A* **2015**, *16*, 8597.

[90] S. Ó. Snæbjörnsdóttir, B. Sigfússon, C. Marieni, D. Goldberg, S. R. Gislason, E. H. Oelkers, *Nat. Rev. Earth Environ.* **2020**, *1*, 90.

[91] E. Mugnaioli, T. Gorelik, U. Kolb, *Ultramicroscopy* **2009**, *109*, 758.

[92] S. Plana-Ruiz, Y. Krysiak, J. Portillo, E. Alig, S. Estradé, F. Peiró, U. Kolb, *Ultramicroscopy* **2020**, *211*, 112951.

[93] R. Vincent, P. A. Midgley, *Ultramicroscopy* **1994**, *53*, 271.

[94] E. Mugnaioli, U. Kolb, *Ultramicroscopy* **2009**, *109*, 758.

[95] L. Palatinus, P. Brázda, M. Jelínek, J. Hrdá, G. Steciuk, M. Klementová, *Acta Crystallogr., Sect. B: Struct. Sci., Cryst. Eng. Mater.* **2019**, *75*, 512.

[96] V. Petříček, M. Dušek, L. Palatinus, *Z. Kristallogr. Cryst. Mater.* **2014**, *229*, 345.

[97] B. H. Toby, R. B. Von Dreele, *J. Appl. Crystallogr.* **2012**, *46*, 544.

[98] P. Juhás, T. Davis, C. L. Farrow, S. J. L. Billinge, *J. Appl. Crystallogr.* **2013**, *46*, 560.